STEEL FIBER REINFORCED SELF-COMPACTING CONCRETE – EXPERIMENTAL RESEARCH AND NUMERICAL SIMULATION

Eduardo N. B. Pereira[1], Joaquim A. O. Barros[2] and Aires Camões[3]

Abstract: Over the last few decades, the astonishing developments of super plasticizers technology allowed great achievements on the conception of concrete mixes exhibiting self-compacting ability. Since the eighties, some methodologies have been proposed to achieve self-compacting requirements in fresh concrete mixes, based on the evaluation of the flowing properties of these mixes. There still persist, however, some doubts about the most appropriate strategy to define the optimum composition of a self-compacting concrete (SCC) mix, based on a required performance. The behavior of SCC as a structural material can be improved if adequate steel fiber reinforcement is added to SCC mix composition. In fact, the fiber reinforcement mechanisms can convert the brittle behavior of this cement based material into a pseudo-ductile behavior up to a crack width that is acceptable under the structural design point-of-view. Fiber addition, however, increases the complexity of the mix design process, due to the strong perturbation effect that steel fibers cause on fresh concrete flow. In the present work, a mix design method is proposed to develop cost effective and high performance Steel Fiber Reinforced Self-Compacting Concrete (SFRSCC). The material properties of the developed SFRSCC are assessed as well as its potentiality as a structural material, carrying out punching and flexural tests on panel prototypes. A material nonlinear analysis is carried out, aiming to address the possibility of calibrating the constitutive model parameters by obtaining, with an inverse analysis, the fracture parameters using force-deflection relationships recorded in simpler laboratory tests, like the three point notched beam bending test. The contribution of steel fibers for punching resistance is also, by this means, discussed.

CE Database subject headings: Self-compacting concrete; Steel fibers; Compression; Flexural; Punching; Finite element method.

[1] Assistant, Dept. of Civil Engineering, Univ. of Minho, Campus de Azurém, 4810-058 Guimarães, Portugal.
E-mail: epereira@civil.uminho.pt; *Corresponding author*
[2] Associate Professor, Dept. of Civil Engineering, Univ. of Minho, Campus de Azurém, 4810-058 Guimarães, Portugal.
E-mail: barros@civil.uminho.pt
[3] Assistant Professor, Dept. of Civil Engineering, Univ. of Minho, Campus de Azurém, 4810-058 Guimarães, Portugal.
E-mail: aires@civil.uminho.pt

Introduction

Self-Compacting Concrete (SCC) can be defined as a concrete that is able to flow in the interior of the formwork, filling it in a natural manner and passing through the reinforcing bars and other obstacles, flowing and consolidating under the action of its own weight (Okamura 1997). SCC was originally developed with the intention of simplifying casting operations in Civil Engineering constructions of large dimensions, where high percentage of reinforcement or complex geometries difficult concrete flow. Soon it became clear, though, that the great productivity increase associated to SCC technology also habilitates it as a good solution for housing construction, precast industry and other applications (Lofgren 2005).

The fresh SCC requirements are mainly resumed to the *filling ability*, the *passing capacity* and the *resistance to segregation*. These properties are evaluated at the mix design stage, based on a series of tests in fresh samples with distinct apparatus (EFNARC 2002). Self-compacting ability in concrete depends on the performance level reached by the fresh mix in these tests.

The introduction of steel fibers in concrete is another issue of interest on the concrete technology. Steel fibers proved to have the potential to increase the post-cracking energy absorption capacity of cement based materials, enhancing the ductile character of concrete structures behavior, mainly of those with high redundant supports (Barros and Figueiras 1998).

The advantages associated to the addition of steel fibers to concrete mixes may be joined with the ones resulting from the self-compacting ability concept in concrete, with the formulation of steel fiber reinforced concrete mixes exhibiting self-compacting ability. The resulting material is, in this work, designated by Steel Fiber Reinforced Self Compacting Concrete (SFRSCC) and, when compared to conventional concretes, presents clear technical advantages in terms of costs/benefits ratio. There exist, however, some drawbacks associated to the SFRSCC formulations, and the most relevant one is related to the strong perturbation effect produced by steel fibers on the flowing ability of fresh concrete. On one side, it is clear that the fluid properties of the fresh SCC formulations are beneficial for the inclusion and homogeneous dispersion of steel fibers. On the other side, steel fibers are rigid and, consequently, do not easily accommodate to the dynamically changing shape of the bulk paste located between the particles constituting the granular skeleton structure. As a result, the design procedure and the optimization technique followed to achieve self-compacting requirements must be sensible to the fiber content, as well as to the geometrical and material properties of the fibers.

In the present work, the procedure followed to develop a cost effective and high performance SFRSCC is briefly described. A detailed exposition can be found elsewhere (Pereira 2006). The hardened SFRSCC

performance in terms of material and structural behavior at early ages is assessed. Compression and flexural tests were carried out with the objective of showing that it is possible to formulate relatively low-cost SFRSCC mixes, exhibiting good mechanical behavior and other relevant properties for structural applications. The developed composition was designed to be applied on the precasting industry, in the fabrication of façade lightweight panels. When compared to the solutions currently used, SFRSCC has some advantages, such as: higher productivity and healthier labor conditions; initial and long term larger toughness; better quality control of the final products; lower costs (Barros *et al.* 2005b). This study also dedicates some attention to the exploration of the structural behavior of SFRSCC lightweight panel prototypes under punching and flexural loading. A smeared crack constitutive model, based on the material fracture parameters and implemented into a computer program (Azevedo *et al.* 2006) able to simulate the material nonlinear behavior of laminar concrete structures, was used to appraise its applicability on the simulation of the punching behavior of SFRSCC panels. The fracture parameters, required to describe the SFRSCC post-cracking constitutive law, were derived from an inverse analysis of the results obtained, for the same material and at the same testing age, at three-point flexural tests in notched prisms. To capture the structural softening behavior observed in the experimental punching tests, a softening diagram for both the out-of-plane shear components in the context of Mindlin shell finite elements theory was implemented.

Mix Design Method

The materials used were cement (C) CEM I 42.5R (rapid hardening and high strength cement, according to EN197-1:2000), limestone filler (LF), a third generation super plasticizer (SP) based on polycarboxylates (Glenium® 77 SCC), water (W), three types of aggregates (fine river sand (FS), coarse river sand (CS) and crushed granite 5-12 mm (CG)) and DRAMIX® RC-80/60-BN hooked end steel fibers. This fiber has a length (l_f) of 60 mm, a diameter (d_f) of 0.75 mm, an aspect ratio (l_f/d_f) of 80 and a yield stress of 1100 MPa.

The methodology followed to formulate the SFRSCC composition is mainly based on the following three steps: i) the proportions of the constituent materials of the binder paste are defined; ii) the proportions of each aggregate on the final granular skeleton are determined; iii) binder paste and granular skeleton are mixed in distinct proportions until self-compacting requirements in terms of spread ability, correct flow velocity, filling ability, blockage and segregation resistance are assured, allowing the determination of the optimum paste content in concrete.

In the first step, a series of tests were performed to achieve the optimum composition of the binder paste. In order to define the optimum percentage of LF in the final composition, several mixes of LF, cement and water were prepared. The proportions of each component were defined in terms of volume, the water content was 66% of fine material (FM) volume, and the percentage of LF has varied between 0% and 125% of the cement volume. To promote the dispersion and deflocculating of the fine particles in suspension, a small constant quantity of super plasticizer was also added to each mix. The relative spread in the "Flow table" and the "Marsh cone" flow time of each mix were measured. The compression strength of each mix was also evaluated on 50 mm edge cubic specimens at an age of 7 days. The results allowed to conclude that a proportion of 100% of LF relative to the cement volume resulted in a good compromise between strength and flowing requirements (Pereira 2006), and also led to an amount of cement on the final concrete mix of approximately 360 kg/m^3.

In the second step, the most appropriate proportions of the three types of aggregates were obtained. Some mixes containing distinct quantities of each type of aggregate were prepared, and a constant volume of 5 dm^3 of each mix was weighted. The optimum aggregate mix was assumed to be the 'heaviest' one, since it should correspond to the most compact. An estimated portion of fibers equivalent to 30 Kg per m^3 of concrete was included in every mixture. Initially, only two of the three types of aggregates were mixed. After finding the optimum proportion between these two, the third aggregate was added in distinct volumetric percentages, keeping constant the proportion between the first two aggregates. The results indicated that the optimum solid skeleton was composed, in volume, by 49.5% of CS, 40.5% of CG and 10% of FS (Pereira 2006).

The third phase was dedicated to the evaluation of the paste content in concrete volume. To achieve the optimum paste content, some mixes of concrete were prepared, varying the paste percentage. For each mix, the added water was corrected taking into account the aggregate's saturation degree. The mix process was always the same, and the slump flow test was performed for each mix. Total spread, *s*, and time to reach a spread diameter of 500 mm, T_{50}, were measured. No visual sign of segregation was detected, the *s* measured value was 720 mm and the mixture showed good homogeneity and cohesion, even while flowing trough the smaller orifice of the Abrams cone (while testing, the Abrams cone was always used in the inverted position). A T_{50} of 3.5 seconds was measured. The composition resulting from this optimization process is represented at Table 1 (the amount of water referred does not includes the aggregate's saturation water).

Mechanical Behavior

The performance evaluation of the designed SFRSCC was based on the assessment of the compression and flexural behavior of hardened SFRSCC. For this purpose, compression and flexural tests were carried out at 5 distinct ages: 12 hours, 24 hours, 3 days, 7 days and 28 days. Cylinder specimens of 150 mm diameter and 300 mm height, and prismatic specimens of 600×150×150 mm^3 were molded without any externally applied compaction energy, for the compression and flexural tests, respectively.

Compression Behavior

The procedure adopted for the assessment of the axial stress-strain relationship of the SFRSCC cylinder specimens was in accordance with the recommendations of ASTM C 39 - 96 (1996). Each test was carried out in a servo-controlled testing machine, with a load carrying capacity of 3000 kN. The test control procedure was defined using the axial displacement as control variable, measured by the internal displacement transducer installed inside the loading equipment. The imposed axial displacement rate was 5 μm/s. The results were obtained from three external displacement transducers disposed at 120º around the specimen, registering the displacement between the two opposite steel load platens. The axial displacement was computed from these results, and then divided by the specimen's initial height to obtain the axial strain. The resulting stress-axial strain curves represented at Fig. 1a correspond to the average load values observed at each strain level, obtained from three specimens at each age. With the results obtained from the three displacement transducers, it was also possible to determine the upper steel load platen rotation at each axial strain (the upper steel load platen was hinged, and the lower one was fixed). In Fig. 1b the average rotation observed at each axial strain, obtained from three specimens, is represented for each age.

Observing the results presented in Fig. 1a, the improvement of the post-cracking compression behavior is apparent at all ages, having in mind the typical shape of the compression stress-axial strain curves for plain concrete. Steel fibers, mainly the ones disposed at a perpendicular direction with respect to the longitudinal cylinder axis, bridge longitudinal cracks and the eventual major inclined crack emerging when the peak load is reached. These additional resisting mechanisms oppose to damage propagation and delay the after peak loss of load carrying capacity. The post-peak load sustaining capacity assured by fiber reinforcement has, however, decreased with the age. This reduction becomes more evident for the ages of 7 days and 28 days. Despite presenting greater peak loads, the specimens tested at 7 days and 28 days ages reveal smaller residual strengths than the younger specimens for greater deformations. This behavior may be interpreted as an indicator of the brittleness increase of concrete matrices with the increase of strength, associated to a reduction of the stress

redistribution capacity and the consequent concentration of deformation in a smaller number of cracks, decreasing the fiber reinforcement effectiveness. Furthermore, the energy released at crack initiation is as high as strong is the matrix. To sustain this energy in a stable fashion, the number of fibers bridging the cracks should accompany the resistance of the matrix. Since the content of fibers remained constant, the load supported by each fiber crossing a crack increased with age, due to the matrix strength increase. For the 7 and 28 days specimens, steel fibers seem to be less efficient on sustaining the specimen load carrying capacity in the post peak stage. This suggests that the load transferred to the fibers at matrix crack initiation over passed a limit load, beyond which the fiber-matrix pullout bond strength mechanisms are affected and their efficacy is reduced.

Referring to the compressive strength evolution in time, it can be observed that a very fast strength gaining with the age occurred, with an average compressive strength of 25 MPa at 12 hours. Taking as reference value the compressive strength at 28 days, the compressive strength evolution at early ages was estimated based on the expression recommended by CEB-FIP Model Code (1993). In Fig. 2a the compressive strength evolution predicted by CEB-FIP expression is compared with the experimental results. In fact, it is apparent that a pronounced compressive strength increase occurs at very early ages. This rapid early age strength gaining might be associated to the type of cement used, a rapid type one. However, this factor was already taken into account on the estimation of the strength gaining evolution by CEB-FIP expressions. Another two factors that may be in the origin of this rapid early strength gaining are the reduced water amount used in the mix and the introduction of large amounts of limestone micro-filler. These two factors, together, may be the cause for the establishment of stronger interactions between the small particles in solution constituting the paste, due to an increase of the proximity between them. As a consequence, the dynamics of the chemical reactions in solution may be changed. Other studies seem to agree on this assumption (Poppe and Shutter 2005).

Looking at the rotation-strain curves presented in Fig. 1b, a relation between the age of the specimens and the rotation levels achieved during compression test seems to exist. In general, younger specimens reached greater rotations. Also, excluding the specimens of 12 hours, all curves seem to agree on the idea that, after an initial phase of adjustment of the upper load platen (up to strains around 0.4‰), the rotation seems to remain constant until the peak load is reached (for strains around 3‰). Then, the rotation at the upper load platen clearly increases with the axial strain increase, up to the end of the test. The rotation of the upper load platen during the compression test may be interpreted as an indicator of the heterogeneity of the specimen. The deformation tends to concentrate at the weakest parts of the specimen, and the heterogeneous distribution of mechanical properties will create heterogeneous deformation, resulting in rotations of the upper load platen. This hypothesis is in

agreement with the results obtained. The greater rotations are observed at the younger specimens, the ones with a greater probability of containing stronger heterogeneities, due to the very early phase of setting and the young stage of formation of its microstructure. It may be observed that for the specimens with 12 hours the rotation is never stabilized, not even prior reaching the peak load, revealing the strong heterogeneities and the weakness of the established microstructure at this age.

The procedure followed to assess the modulus of elasticity (E_c) of the SFRSCC specimens was mainly based on RILEM TC14-CPC8 (1975), and on ASTM C 469 - 94 (1994). The tests were carried out in the same equipment used to obtain the compression stress-strain relationships. The test control procedure was defined using the axial load as control variable, measured by the internal load cell included on the upper plate of the loading equipment. The prescribed loading sequence consisted on three loading-unloading cycles, with the load value varying between an upper level of one third of the estimated compressive strength at each age, and the lower level of 0.5 MPa. The final value of the elasticity modulus was obtained for each specimen by dividing the stress difference between loading and unloading cycles, by the strain difference observed in the last unloading cycle. The average values of the elasticity modulus, obtained at each age, and the scatter of the corresponding results are depicted in Fig. 2b.

As a reference, the elasticity modulus was estimated for plain concrete at each age based on the CEB-FIP expressions, using the results obtained for compressive strength and admitting the granitic nature of the aggregates. The results are depicted in Fig. 2b and, when compared to the experimental ones, it is apparent that both curves present a similar shape, but the magnitude of values is clearly different. The SFRSCC showed higher deformability than expected for a conventional plain concrete mix, at all tested ages. The main reason for the greater deformability observed in SFRSCC may reside on the much greater paste contents typically present in self-compacting concrete mixes than in the conventional concretes. Since aggregates are much less deformable than hardened paste, in a hardened composition with higher paste contents the deformability is obviously higher (van Mier 1984). The values of the compressive strength and the elasticity modulus of each carried test are referred elsewhere (Pereira 2006).

Flexural Behavior

To evaluate the flexural tensile behavior of the developed SFRSCC, simply supported notched beams were tested under three-point loading conditions, according to the recommendations of RILEM TC 162-TDF (2002). Four prismatic specimens of 150 × 150 mm^2 cross section and a length of 600 mm were tested at each of the five

studied ages. The notch at midspan was produced on one of the faces perpendicular to the casting surface, using wet sawing. The width of the notch was 3 mm, and the depth 25 mm, leaving a section with a net depth (h_{sp}) of 125 mm at midspan. The distance between the two roller supports was 500 mm, and the deflection was measured at midspan with a displacement transducer.

The tests were carried out with closed-loop testing equipment, using as control variable the deflection at midspan. The displacement at midspan was steadily increased with a displacement rate of 1 μm/s. After reaching a midspan deflection of 0.1 mm, the displacement rate was increased to 3 μm/s. Testing procedure was stopped when a total deflection at midspan of 3 mm was reached. The smaller deformation velocity imposed to the specimen at the beginning of the testing sequence had the purpose of avoiding test instabilities due to crack initiation at the matrix. The results obtained at each of the five testing ages are represented in Figs. 3a and 3b. Each curve represents the average load at each midspan deflection, measured in 4 specimens at each age. It can be observed that, as a result of the tensile strength increase of concrete matrix with age, the load at the limit of proportionality (F_L), corresponding to the maximum load reached up to a deflection of 0.05 mm (RILEM TC 162-TDF 2002), clearly increased with age. In a following stage, for deflections between 0.05 mm and 0.2 mm, a slight decay of the load carrying capacity occurs for all ages, but this reduction assumes greater relevance with age. At this stage, the equilibrium at the onset of matrix cracking is achieved by the migration of the tensile stresses from concrete matrix to the steel fibers. With the increase of the concrete matrix tensile strength with age, the tensile stress resultant that has to be absorbed by steel fibers during cracking increases. Assuming a constant amount of steel fibers for all ages, the force transferred to each steel fiber increases with concrete age, justifying the observed increasing load decay with the age, at this stage. After the overcome of this transition stage, a new stage of increasing load carrying capacity is observed at all ages, for deflections greater than 0.2 mm, due to an effective contribution of steel fibers for the toughening mechanisms in concrete matrix. An exception is found, though, at the 28 days age, exhibiting the load-deflection curve a very slight strength increase when compared to the other curves, followed by pronounced load decay. Starting at an approximate deflection of 1.0 mm, this load decay gradually leads to an intersection with all the other 4 curves, terminating at a deflection of 3 mm with a much lower residual strength than any other. The increase on tensile strength of the concrete matrix with the age is probably, once more, the main reason justifying these results. For the 28 days specimens, due to the transference of a significant load from matrix to fibers at the onset of matrix cracking, damages occur on fiber-matrix bond mechanisms, irremediably affecting the toughness efficacy provided by steel fibers. For this level of transferred load, the number of fibers seems to be insufficient to guarantee a fiber

slip below the slip at fiber peak pull-out force, i.e., in the ascending branch of the fiber-matrix bond stress-slip relationship, τ_f -s_f (Robins *et al.* 2002). As a result, the steel fibers located just above the notch entered in the softening phase of the τ_f-s_f behavior, conferring a flexural softening behavior to the notched beams.

For the tested specimens, the values of the parameters proposed by RILEM TC 162-TDF (2002) to define the flexural behavior of SFRC can be found elsewhere (Pereira 2006)

Structural Behavior

As already mentioned, steel fiber reinforcement is particularly efficient in structures with redundant number of supports, since high stress redistribution occurs after concrete crack initiation. In this context, SFRSCC panel prototypes were tested under punching and bending setup conditions, allowing the evaluation of the SFRSCC behavior under the two most demanding loading conditions for the façade panels. The punching tests were executed in panel prototypes of 600 × 600 mm^2 and 110 mm thick, and the flexural tests were carried out in panel prototypes of 1000 × 1000 mm^2 and the same thickness, both at an age of 7 days.

Punching Test in Panel Prototype

As represented in Fig. 4a, the lightweight central region of the panel prototype subjected to punching load is composed by a concrete layer of 30 mm thick. The procedure followed to assess the load-deflection behavior of the lightweight SFRSCC panel prototype consisted on applying a load at the centre of the panel, by means of a square steel plate of 100 mm edge and 10 mm thick. The loading sequence was executed using the vertical displacement as control variable, measured by the internal displacement transducer included on the loading equipment. A vertical displacement rate of 25 μm/s was prescribed, and the testing procedure was stopped when punching failure was observed. The results obtained in terms of load-deflection curve are represented in Fig. 4b. After a short linear elastic phase, the panel entered into an elastic-cracked phase and supported an increasing load up to 40 kN. This load level was then maintained practically constant from a deflection of 1.4 mm up to a deflection of about 3 mm, representing 1% of the lightweight zone span. Then, the load suddenly falls from the 40 kN to approximately 20 kN, suggesting the occurrence of failure by punching. Fibers bridging the surfaces of the punching failure crack offered some resistance to the opening of this crack, delaying the loss of contribution of the aggregate interlock for the punching resistance. This justifies the relatively high level of residual strength that decreases very slowly with the deflection increase. The estimation of the steel fibers contribution for punching strength increase is further discussed in a subsequent section.

Flexural Test in Panel Prototype

The panel prototype destined for the evaluation of flexural behavior was conceived using the same lightweight concept as in punching. As represented in Fig. 5a, lightweight zones had also a concrete upper layer of 30 mm thick, and the thicker zones of the panel constituted a grid system of two-per-two orthogonal ribs. The panel has also a contour rib of 100 mm width. The test procedure consisted on applying a constant displacement rate (25 μm/s) at the centre of a main loading steel beam, connected to other two transversal secondary beams by means of two rollers. Load was transmitted to the four loading points at rib intersections by means of four square steel plates (100×100×20 mm^3) and four steel spheres of 20 mm diameter, in contact with the ends of the secondary loading beams. This entire loading mechanism was idealized with the intention of assuring that, independently of the deflection observed beneath each of the four loading points, the applied load was the same in each loaded area. To obtain the vertical deflection beneath each of these four loaded areas, four displacement transducers were there installed. The supports system was constituted by eight elements placed at the ends of the grid ribs. Each of these elements was constituted by a steel plate (100×100×10 mm^3) in contact with the lower surface of the panel, and a steel sphere of 20 mm diameter, placed between the steel plate and the ground, guaranteeing that only the vertical displacement was constrained (lifting was not prevented). The results obtained in terms of load-deflection curve are represented in Fig. 5b, showing that the load bearing retaining capacity of the structure assumes relevance, in similitude to the results observed at punching tests. To simplify the analysis, only the average results will be considered. After reaching a peak load of approximately 55 kN, the panel demonstrates the ability to almost totally retain the load carrying capacity up to an average deflection of around 5 mm. Even then, the load carrying capacity decreases very slowly with the average deflection increase, and the testing sequence is stopped for a load of 15 kN (27% of the peak load) due to excess of deformation and incompatibility with the supports and the loading apparatus.

Modeling

The prediction of the deformational behavior of a structure made with the developed SFRSCC may be a complicated problem to solve. Nowadays, several finite element approaches, of a continuum or discrete nature, are suggested to analyze, with distinct degrees of precision, the material/structural behavior of complex structures subjected to the most distinct load cases. The most recent ones reveal particular efficiency on modeling concrete brittle failure of complex loading configurations, with a very precise prediction of crack

formation and progression. Discrete cohesive fracture models (discrete) with fragmentation algorithms, strong discontinuity approaches (continuum) with the embedded discontinuities method and the extended finite element method are examples of advanced methodologies that, together with powerful mesh refinement algorithms, reveal great efficiency on modeling concrete brittle failure (Yu RC et al. 2007). Other solutions may be found on the damage models, smeared crack models and micro-plane models, less precise on the prediction of the crack emergence and propagation during concrete failure, but more appropriate to analyze large structures with a great number of degrees of freedom. As demonstrated by (De Borst 2002), "*fixed or rotating smeared crack models and micro-plane models may be considered as a special case of (anisotropic) damage models*", so these last three FEM solutions are closely related and produce analogous results. In the context of this work, the main idea of this section is to demonstrate that it is possible to predict, with good approximation, the failure behavior of SFRSCC laminate structures by using the material fracture parameters obtained from inverse analysis of a simple laboratory test, the tree point notched beam bending test (Barros et al. 2005a, Sena-Cruz et al. 2004). From the abovementioned models, the multi-fixed smeared crack was the selected one, since it allows the analysis of large scale SFRSCC structures (De Borst, 1987, Rots 1988, Dahlblom and Ottosen 1990), as long as an appropriate constitutive law is used for modeling the SFRSCC post-cracking behavior. In the present case, the structural aspect of the analysis of the deformational behavior of laminar structures was resolved by employing the theory of plane shells, based on the 'Reissner-Mindlin' formulation (Barros 1995).

FEM Constitutive Model

Considering that the stress state in concrete is related, at each instant, with the strain state by a constitutive law, the matrix relating them is known as the constitutive matrix:

$$\begin{bmatrix} \Delta\underline{\sigma}_{mf} \\ \underline{\sigma}_{s} \end{bmatrix} = \begin{bmatrix} \underline{D}_{mf}^{crco} & \underline{0} \\ \underline{0} & \underline{D}_{s}^{crco} \end{bmatrix} \begin{bmatrix} \Delta\underline{\varepsilon}_{mf} \\ \underline{\varepsilon}_{s} \end{bmatrix} \tag{1}$$

where $\Delta\underline{\sigma}_{mf} = \left\{\Delta\sigma_x, \Delta\sigma_y, \Delta\tau_{xy}\right\}^T$ and $\Delta\underline{\varepsilon}_{mf} = \left\{\Delta\varepsilon_x, \Delta\varepsilon_y, \Delta\gamma_{xy}\right\}^T$ are the vectors of the increment stress and increment strain in-plane components, and $\underline{\sigma}_s = \left\{\tau_{yz}, \tau_{zx}\right\}^T$ and $\underline{\varepsilon}_s = \left\{\gamma_{yx}, \gamma_{zx}\right\}^T$ are the vectors of the total stress and total strain shear out-of-plane components, respectively.

Due to a decomposition of total strain into an elastic concrete part and a crack part ($\varepsilon^{crco} = \varepsilon^{co} + \varepsilon^{cr}$), in Eq. (1) the in-plane cracked concrete constitutive matrix, $\underline{D}_{mf}^{crco}$, is obtained by performing the following matrix operations (Sena-Cruz 2004):

$$\underline{D}_{mf}^{crco} = \underline{D}_{mf,e}^{co} - \underline{D}_{mf,e}^{co}\left[\underline{T}^{cr}\right]^{T}\left(\underline{D}^{cr} + \underline{T}^{cr}\,\underline{D}_{mf,e}^{co}\left[\underline{T}^{cr}\right]^{T}\right)^{-1}\underline{T}^{cr}\,\underline{D}_{mf,e}^{co} \tag{2}$$

where $\underline{D}_{mf,e}^{co}$ is the constitutive matrix for linear-elastic concrete:

$$\underline{D}_{mf,e}^{co} = \frac{E_c}{1-\nu^2}\begin{bmatrix} 1 & \nu & 0 \\ \nu & 1 & 0 \\ 0 & 0 & \dfrac{1-\nu}{2} \end{bmatrix} \tag{3}$$

with E_c and ν being the elasticity modulus and the Poisson ratio for the concrete. In Eq. (2) $\underline{T}^{cr}$ represents the matrix that transforms the stress components from the coordinate system of the finite element to the crack local coordinate system:

$$\underline{T}^{cr} = \begin{bmatrix} \cos^2\theta & \sin^2\theta & 2\sin\theta\cos\theta \\ -\sin\theta\cos\theta & \sin\theta\cos\theta & \cos^2\theta - \sin^2\theta \end{bmatrix} \tag{4}$$

and $\underline{D}^{cr}$ is the crack constitutive matrix:

$$\underline{D}^{cr} = \begin{bmatrix} D_I^{cr} & 0 \\ 0 & D_{II}^{cr} \end{bmatrix} \tag{5}$$

In the Eq. (4), θ is the angle between x_1 and n (see Fig. 6a). In the Eq. (5) D_I^{cr} and D_{II}^{cr} represent, respectively, the constitutive components relative to the crack opening mode I (normal) and mode II (in-plane shear).

The softening nature of the crack opening propagation is simulated by the tri-linear diagram represented in Fig. 6b, which is defined by α_i and ξ_i parameters, relating stress and strain at the intersection points between linear intervals. The ultimate crack strain ($\varepsilon_{n,ult}^{cr}$) is defined as a function of α_i and ξ_i parameters, and of the fracture energy (G_f^I), the tensile strength (f_{ct}) and the crack band width (l_b), as follows (Barros 1995):

$$\varepsilon_{n,ult}^{cr} = \frac{2}{\xi_1 + \alpha_1\xi_2 - \alpha_2\xi_1 + \alpha_2} \cdot \frac{G_f^I}{f_{ct} l_b} \tag{6}$$

where $\alpha_1 = \sigma_{n,2}^{cr} / \sigma_{n,1}^{cr}$, $\alpha_2 = \sigma_{n,3}^{cr} / \sigma_{n,1}^{cr}$, $\xi_1 = \varepsilon_{n,2}^{cr} / \varepsilon_{n,u}^{cr}$ and $\xi_2 = \varepsilon_{n,3}^{cr} / \varepsilon_{n,u}^{cr}$.

The fracture mode II modulus, D_{II}^{cr}, is obtained from,:

$$D_{II}^{cr} = \frac{\beta}{1-\beta} G_c \tag{7}$$

$$\beta = \left(1 - \frac{\varepsilon_n^{cr}}{\varepsilon_{n,u}^{cr}}\right)^{p_1} \tag{8}$$

where β is known as the shear retention factor, defined as a function of the actual crack normal strain (ε_n^{cr}) and the ultimate crack normal strain ($\varepsilon_{n,u}^{cr}$). If a linear decrease of β with the increase of ε_n^{cr} is assumed, p_1=1. Higher degradation of β can be attributed if larger values are taken for p_1 (Barros 1995). In Eq. (7) G_c is the concrete transverse elasticity modulus. The use of an independent softening constitutive law to model the in-plane crack shear stress transfer was also experimented in the ambit of the present research, but its adoption in detriment of the simple concept reflected in Eq. (8) did not contribute to increase the accuracy of the numerical simulations, and the difficulties on assuring convergence in the Newton-Raphson iterative procedure increased significantly.

The diagram represented in Fig. 6c was used to simulate the out-of-plane constitutive matrix, $\underline{D}_s^{crco}$ in Eq. (1). When the portion of concrete associated with the integration point (IP) changes from uncracked to cracked state, the out-of-plane shear stresses are stored and the relation between each out-of-plane shear stress-strain ($\tau_{yz} - \gamma_{yz}$ and $\tau_{zx} - \gamma_{zx}$) follows the softening relation depicted in Fig. 6c. Therefore, the $\underline{D}_s^{crco}$ matrix is defined by

$$\underline{D}_s^{crco} = \begin{bmatrix} D_{III,\sec}^{yz} & 0 \\ 0 & D_{III,\sec}^{zx} \end{bmatrix} \tag{9}$$

where,

$$D_{III,\sec}^{yz} = \frac{\tau_{yz,\max}}{\gamma_{yz,\max}},\ D_{III,\sec}^{zx} = \frac{\tau_{zx,\max}}{\gamma_{zx,\max}} \tag{10}$$

according to a secant approach (see Fig. 6c). For each out-of-plane shear component, the peak shear strain is calculated using both the stored peak shear stress at crack initiation and G_c:

$$\gamma_{yz,p} = \frac{\tau_{yz,p}}{G_c}, \gamma_{zx,p} = \frac{\tau_{zx,p}}{G_c} \tag{11}$$

Each out-of-plane ultimate shear strain is defined as a function of the out-of-plane peak shear strain (γ_p^{OP}), the out-of-plane shear strength (τ_p^{OP}), the mode III (out-of-plane) fracture energy (G_f^{III}) and the crack bandwidth (l_b), as follows:

$$\gamma_{yz,u} = \gamma_{yz,p} + \frac{2G_f^{III}}{\tau_{yz,p}\, l_b}, \quad \gamma_{zx,u} = \gamma_{zx,p} + \frac{2G_f^{III}}{\tau_{zx,p}\, l_b} \tag{12}$$

In the present approach it is assumed that the crack bandwidth used for assuring mesh independence when modeling fracture mode I can also be used to define the dissipated energy in the out-of-plane fracture process.

Mode I Fracture Properties from Inverse Analysis

As abovementioned, the post-cracking behavior of hardened SFRSCC in tension is, in this work, described by a tri-linear stress-strain softening diagram. The shape of this function is defined by a group of fracture parameters (α_i, ξ_i, G_f, f_{ct} and l_b) and the accuracy of the FEM modeling largely depends on the values defined for each of these parameters. In this context, the obtained experimental results of punching test may be predicted by a FEM model, if the correct values of the material fracture parameters are found and introduced in the constitutive model. The question is, though, what is the best strategy to obtain the accurate values for these parameters.

In this work, it is suggested that the fracture parameters may be assessed by means of an inverse analysis of the flexural test results, in agreement with previous studies (Sena-Cruz *et al.* 2004). The procedure consists on the evaluation of the ξ_i, α_i and G_f^I parameters, the ones that define the shape of the tri-linear $\sigma_n^{cr} - \varepsilon_n^{cr}$ constitutive law, leading to the minimization of the ratio between the area limited by the experimental and the numerical curves and the area underneath the experimental curve. The experimental curve corresponds to the average results observed in prismatic SFRSCC notched specimens, tested according to the RILEM TC 162-TDF recommendation, at the age of 7 days. The numerical curve consists on the results obtained by means of a FEM analysis (see Fig. 7a), where the specimen, the loading and the support conditions were simulated in agreement to the experimental flexural test setup. In this context, the specimen was modeled by a mesh of 8 node ´serendipity' plane stress finite elements. The Gauss-Legendre integration scheme with 2×2 *IP* was used in all elements, with the exception of the elements at the specimen symmetry axis, where only 1×2 *IP* were used. This had the purpose of producing a trend to the development of the crack line along the specimen symmetry axis, over the aligned integration points, in agreement with the experimentally observed. Linear elastic material behavior was assigned to all elements, with the exception of the elements above the notch and along the specimen symmetry axis, where elastic-cracked behavior in tension was assumed. The crack band width, l_b, was assumed to be 5 mm, equal to the width of the notch and of the elements above.

In Fig. 7b, the results obtained experimentally for flexural tests are compared with the ones resulting from the numerical model of the same test setup. The numerical curve, obtained with the optimized fracture parameters, is not exactly equal to the experimental one, suggesting that more parameters would have to be introduced in order to attain better fitting. Despite not being perfect, there exists, though, a very good agreement between the experimental and the numerical curve. The values assumed for the fracture parameters, ξ_i, α_i and G_f^I, that resulted in the obtained numerical curve represented in Fig. 7b, are presented in table 2.

Punching Test Simulation

The experimental results recorded from punching test of the panel prototype are compared with the ones obtained from the numerical simulation model. For this purpose, a FEM mesh was prepared, composed by 12 per 12 eight-node serendipity plane shell elements, each one divided in 11 layers 10 mm thick. Reminding that the panel had lightweight zones, materialized by the suppression of 80 mm of concrete at a 300×300mm^2 square central area, the 8 lower layers of the finite elements at the lightweight central square were constituted by a fictitious material with numerically null rigidity. The remaining three upper layers, and all layers of the elements located outside the lightweight zone, were constituted by the material defined in the model as 'SFRSCC', assigned with elastic-cracked type of material behavior, in accordance with the model above described.

The out-of plane component of the elastic-cracked constitutive matrix ($\underline{D}_s^{crco}$) was defined on the basis of a trial-and-error procedure. The out-of-plane shear fracture energy value that best fitted the punching failure experimental results ($G_f^{III} = 3.0\,N/mm$) was determined in this fashion, since no other laboratory test was carried out to allow its assessment by inverse analysis. To define the in-plane component elastic-cracked constitutive matrix for concrete ($\underline{D}_{mf}^{crco}$), the fracture parameters defining D_I^{cr} of $\underline{D}^{cr}$ had to be established. To verify the adequacy of an indirect evaluation, these fracture parameters were assumed to be equal to the ones obtained by inverse analysis of the experimental results of flexural tests, for the same concrete composition and at the same age. The results obtained form the numerical model were compared with the experimental ones in Fig. 4b. A quite good simulation was obtained up to a deflection of 2.5 mm. For greater deflections, it is clear an over-estimation of the load carrying capacity of the prototype panel, if a linear elastic behavior is assumed for the out-of-plane shear components. At an approximate deflection of 3 mm, the load at the experimental curve suddenly falls, indicating the failure of the panel by punching, as visually found during experimental testing. This load decay, not possible to be simulated by assuming linear elastic behavior for the out-of-plane shear

components was, however, well captured by the numerical simulation when the bilinear function represented in Fig. 6c was used to model the softening behavior of out-of-plane shear components, with $G_f^{III} = 3.0\,N/mm$ and assuming a crack band width l_b equal to the square root of the area of the corresponding integration point. The abrupt load decay form approximately 42 kN to 25 kN observed experimentally was almost perfectly followed by the numerical model, as well as the observed subsequent long stage of residual strength retaining, presenting a very slow decay.

When analyzing the initial part of the experimental and numerical curves, a very good agreement exists between them. However, the deformational behavior predicted by a linear elastic analysis starts diverging from the curves corresponding to the experimental recordings and material nonlinear analysis since very early stage of the panel deformation. These results suggest that cracks start to appear in concrete at a very early stage during testing. By analyzing the crack patterns resulting from the numerical model, the emergence of bending cracks at the upper face of the panel is detected by the model (see Fig. 8a), in agreement with the experimentally observed. These cracks initiate at the central region of the four edges constituting the 300×300 mm^2 square border limiting the lightweight central zone, at the upper face. Fig. 8b shows the total development of the crack at the upper face of the panel, verified experimentally after the end of the test sequence. The numerical model also indicates the emergence of bending cracks at the lower panel surface, in the lightweight zone. These cracks initiate at the center of the panel, beneath the loaded area loading point, and then develop in the direction of the corners of the lightweight zone, in similitude to the typical yield lines formed at square concrete slabs failing by flexure (these cracks were also detected experimentally). In conclusion, it may be assumed that flexure mechanisms prevail in the deformational behavior up to an approximate deflection of 2.5 mm. For greater deflections, the punching failure mechanisms start to assume greater relevance, and the overestimation of the panel out-of-plane rigidity components when linear out-of-plane shear behavior is assumed leads the numerical model to diverge from the experimental results. With the adoption of a softening law also for the out-of-plane shear components, the model shows very good accuracy on predicting the entire behavior of the panel failing in punching, capturing with precision the sudden load decay associated to punching failure mechanisms.

Estimation of Fibers Contribution for Punching Behavior

In order to estimate the contribution of steel fibers for punching strength increase on panel prototype, the results obtained for the SFRSCC would have to be compared with the ones obtained from a plain concrete panel prototype. As discussed in a previous work (Pereira 2006), it is not possible to isolate the effect of the steel fibers

in a concrete mix, since the granular skeleton composition was optimized on the presence of the steel fibers in use. The simple exclusion of steel fibers creates changes on the structural arrangement of the granular skeleton, and, consequently, the mechanical behavior changes, not only due to the absence of the steel fibers, but also due to the new and different granular skeleton particles arrangement.

The strategy proposed here to estimate the contribution of steel fibers for punching behavior is based on the establishment of a softening stress-strain law diagram for plain concrete in tension. The remaining characteristics of the numerical simulation were the same ones as used on the previous SFRSCC material nonlinear analysis. The softening stress-strain law for plain concrete in tension was established in accordance with (CEB-FIP 1993) recommendations. Assuming that the tensile strength is the same for SFRSCC matrix and for the equivalent plain concrete, the fracture parameters defining a bilinear stress-strain diagram ($D_{I,2}^{cr} = D_{I,3}^{cr}$ in Fig. 6b) were determined, and are indicated in Table 2. Fig. 4b represents the predicted deformational behavior of a plain concrete panel prototype, from which it can be observed that plain concrete has a punching strength that is around 70% of the punching strength of SFRSCC, and the energy absorbed up to the failure of plain concrete panel represents only around 15% of the energy absorbed by SFRSCC panel.

Conclusions

In the present work an innovative mix design method was proposed to develop cost effective and high performance steel fiber reinforced self-compacting concrete (SFRSCC). The amount of cement did not exceed 360 kg per m^3 of concrete. For an amount of 30 kg of hooked end steel fibers (60 mm in length and 0.75 mm in diameter) per m^3 of concrete, a total spread of 720 mm and a time of 3.5 seconds to reach a spread diameter of 500 mm were obtained, indicating that the optimized SFRSCC mix exhibited self-compacting ability. At 12 hours the average cylinder compressive strength (f_{cm}) had already exceeded 25 MPa and attained an f_{cm} of about 62 MPa at 28 days. During compression tests, a significant residual strength was recorded for large specimen axial deformation. However, this capability decreased with the age of the specimens, since a too large amount of energy is released at crack initiation of the strong matrix of 7 and 28 days SFRSCC specimens, facing the constant fiber content applied.

Three point notched SFRSCC beams were tested according to the recommendations of RILEM TC 162-TDF at five distinct ages to assess the flexural tensile behavior of the developed SFRSCC. The limit of proportionality, F_L, increased with the SFRSCC age, as well as the maximum load and the energy absorption capacity. However, SFRSCC specimens of 28 days showed much more pronounced load decay in the softening

phase than the specimens of the other ages. The amount of fibers crossing the fracture surface of SFRSCC 28 days' specimens of relatively high tensile strength was not enough to sustain, in a stable mode, the resultant tensile stresses transferred from matrix to fibers at matrix crack initiation. To sustain in identical levels the residual strength of specimens of increasing tensile strength, the fiber content should be increased. The force-deflection relationships recorded in the notched SFRSCC beam tests were also used to assess, from inverse analysis, the fracture mode I parameters of this composite material. The values of these parameters were used to characterize the fracture mode I of a smeared crack constitutive model adopted to simulate the behavior of a SFRSCC panel prototype tested under punching load conditions, in the framework of the finite element material nonlinear analysis. This numerical strategy allowed simulating with high accuracy the loading-deformational process of the experimentally tested panel that failed in a brittle manner, by punching. Successful applications of this model to study the failure behavior of large scale laminar structures may be anticipated, given the good results obtained. The main aspects of the crack pattern were also reproduced numerically. Performing a numerical analysis of a panel of plain concrete "equivalent" to SFRSCC, it was verified that fibers assure an increase on the punching resistance of about 43% and an increase of about 6 times the energy absorption capacity.

The benefits of fiber reinforcement were also visible in panel prototypes of redundant number of supports and failing in bending. The maximum load was significantly larger than the load at matrix crack initiation, and this load was practically maintained up to a panel central deflection of about 5 mm. Above this deflection, the fibers crossing the various formed cracks allowed a smooth decrease of the panel load carrying capacity.

Acknowledgements

The study reported in this paper is part of the research program "Prefabricated sandwich steel fiber reinforced panels" supported by FEDER and MCT, and promoted by ADI (the funds was 45% of the applied amount). This project involves the Companies PREGAIA and CIVITEST, and the University of Minho. The authors wish to acknowledge the materials generously supplied by Bekaert (fibers), SECIL (cement), Degussa (superplasticizer), and Comital (limestone filler).

Notation

C = cement

CG = crushed granite

CS = coarse river sand

$\underline{D}$ = constitutive matrix

$\underline{D}^{cr}$ = crack constitutive matrix

D_I^{cr} = crack constitutive matrix component relative to the crack normal opening mode (mode I)

D_{II}^{cr} = crack constitutive matrix component relative to the crack in-plane sliding mode (mode II)

$D_{III,\sec}^{yz}$ = constitutive matrix component yz relative to the out-of-plane sliding mode (mode III)

$D_{III,\sec}^{zx}$ = constitutive matrix component zx relative to the out-of-plane sliding mode (mode III)

$\underline{D}_{mf,e}^{co}$ = constitutive matrix in-plane components for concrete in elastic regime

$\underline{D}_{s,e}^{co}$ = constitutive matrix out-of-plane components for concrete in elastic regime

$\underline{D}_{mf}^{crco}$ = constitutive matrix in-plane components for cracked concrete

$\underline{D}_{s}^{crco}$ = constitutive matrix out-of-plane shear components for cracked concrete

E_c = concrete elasticity modulus

F = shear corrective factor

F_L = load at the limit of proportionality for three point notched beams flexural tests

FS = fine sand

G_c = concrete transverse elasticity modulus

G_f^I = fracture energy (mode I)

G_f^{III} = fracture energy (mode III)

IP = integration points

LF = limestone filler

SCC = self compacting concrete

$SFRC$ = steel fiber reinforced concrete

$SFRSCC$ = steel fiber reinforced self compacting concrete

SP = super plasticizer

T_{50} = time to reach a spread diameter of 500 mm on the spread flow test

$\underline{\underline{T}}^{cr}$ = transformation matrix from crack local coordinate system to element local coordinate system

W = water

d_f = steel fiber diameter

f_{ct} = tensile strength

h_{sp} = midspan section net depth at three point notched beams flexural test

l_b = crack band width

l_f = steel fiber length

p_1 = shear degradation factor

s = total spread measured on the spread flow test

β = shear retention factor

ε_n^{cr} = crack normal strain

$\varepsilon_{n,ult}^{cr}$ = ultimate crack normal strain

θ = angle between the crack local coordinate system and the element local coordinate system

γ^{OP} = generic out-of-plane shear strain.

γ_{yz} = out-of-plane shear strain (yz component).

$\gamma_{yz,p}$ = out-of-plane peak shear strain (yz component).

$\gamma_{yz,u}$ = out-of-plane ultimate shear strain (yz component).

γ_{zx} = out-of-plane shear strain (zx component).

$\gamma_{zx,p}$ = out-of-plane peak shear strain (zx component).

$\gamma_{zx,u}$ = out-of-plane ultimate shear strain (zx component).

ξ_i = fracture parameters used to define the tri-linear stress-strain softening diagram

$\underline{\sigma}_{mf}$ = in-plane stress components

σ_n^{cr} = crack normal stress

$\underline{\sigma}_s$ = out-of-plane stress components

τ^{OP} = generic out-of-plane shear stress.

τ_{yz} = out-of-plane shear stress (yz component).

$\tau_{yz,p}$ = out-of-plane peak shear stress (yz component).

$\tau_{yz,u}$ = out-of-plane ultimate shear stress (yz component).

τ_{zx} = out-of-plane shear stress (zx component).

$\tau_{zx,p}$ = out-of-plane peak shear stress (zx component).

$\tau_{zx,u}$ = out-of-plane ultimate shear stress (zx component).

υ = poisson coefficient

References

ASTM C 39 - 96. (1996). “Standard test method for compressive strength of cylindrical concrete specimens.” *Annual book of ASTM Standards*, 04.02: 18–22.

ASTM C 469 – 94. (1994). “Standard test method for static modulus of elasticity and poisson’s ratio of concrete in compression.” *Annual book of ASTM Standards*, 04.02: 238–41.

Azevedo, A.F.M., Barros, J.A.O., and Sena-Cruz, J.M. (2006). “FEMIX - Computer program for the linear and nonlinear structural analysis.” *Dep. Civil Eng. Univ. of Minho*, <http://www.civil.uminho.pt/composites/Software.htm>

Barros, J.A.O., Cunha, V.M.C.F., Ribeiro, A.F., and Antunes, J.A.B. (2005a). “Post-Cracking Behaviour of Steel Fibre Reinforced Concrete", *RILEM Materials and Structures Journal*, 38(275), 47-56.

Barros, J.A.O. ; Pereira, E.B.; Cunha, V.M.C.F.; Ribeiro, A.F.; Santos, S.P.F. and Queirós, P.A.A.A.V. (2005b). “PABERFIA- Lightweight sandwhich panels in steel fiber reinforced self compacting concrete." *Technical Report 05-DEC/E-29*, Dep. Civil Eng., School Eng. University of Minho, 63 pp.

Barros, J.A.O., and Figueiras, J.A. (1998). “Experimental behaviour of fiber concrete slabs on soil.” *Journal Mechanics of Cohesive-frictional Materials*, 3, 277-290.

Barros, J.A.O., (1995). “Behaviour of fibre reinforced concrete – numerical and experimental research.” PhD Thesis, Civil Eng. Dept., Faculty of Eng., Univ. of Porto, Portugal. (in Portuguese)

CEB-FIP Model Code 1990. (1993) “Design Code.” Comite *Euro-International du Béton*, Bulletin d’Information nº 213/214, 437 pp.

Dahlblom, O. and Ottosen, N.S. (1990). “Smeared crack analysis using generalized fictitious crack model.” *Jour. of Eng. Mech.*, ASCE, 116(1), 55-76.

De Borst, R. (1987). “Smeared cracking, plasticity, creep and thermal loading - a unified approach.” *Comp. Meth. Appl. Mech. Eng.*, 62, 89-110.

De Borst, R. (2002). “Fracture in quasi-brittle materials: a review of continuum damage-based approaches.” *Eng Fract Mech, 69, 95-112.*

EFNARC (2002). “Specification and Guidelines for Self-Compacting Concrete.” ISBN 0 9539733 4 4, 32 pp.

EN197-1:2000 (2000). “Cement. Composition, specifications and conformity criteria for low heat common cements.” ISBN: 058036456 9, 52pp.

Lofgren, I. (2005). “Fibre-reinforced Concrete for Industrial Construction.” PhD Thesis, Department of Civil and Environmental Engineering, Chalmers University of Technology, Sweden.

Okamura, H. (1997). “Ferguson Lecture for 1996: Self-compacting high-performance concrete.” Concrete International, ACI 19(7), 50-4.

Pereira, E.N.B. (2006). “Steel Fibre Reinforced Self-compacting Concrete: from material to mechanical behaviour”, dissertation for Pedagogical and Scientific Aptitude Proofs, Department Civil Engineering, University of Minho, 188 pp, <http://www.civil.uminho.pt/composites>

Poppe, A. and Shutter, G. D. (2005). “Cement hydration in the presence of high filler contents.” *Cement and Concrete Research*, 35, 2290–2299.

RILEM TC 14-CPC8 (1975). “Modulus of elasticity of concrete in compression: final recommendation.” *Materials and Structures*, 6(30), 25–27.

RILEM TC 162-TDF (2002). “Test and design methods for steel fibre reinforced concrete - Final Recommendation.” *Materials and Structures* 35(253), 579-582.

Robins, P, Austin, S., and Jones, P. (2002). "Pull-out behaviour of hooked steel fibres." *Materials and Structures*, 35(251), 434-442.

Rots, J.G. (1988). “Computational modeling of concrete fracture.” PhD Thesis, Delft University of Technology.

Sena-Cruz, J.M. (2004). “Strengthening of concrete structures with near-surface mounted CFRP laminate strips.” PhD Thesis, Department of Civil Engineering, University of Minho, <http://www.civil.uminho.pt/composites>

Sena-Cruz, J.M.; Barros, J.A.O.; Ribeiro, A.F.; Azevedo, A.F.M., and Camões, A.F.F.L. (2004). "Stress-crack opening relationship of enhanced performance concrete." *9th Portuguese Conference on Fracture, ESTSetúbal*, Portugal, 395-403.

van Mier, J.G.M. (1984). “Strain Softening of Concrete under Multiaxial loading conditions.” Ph.D. thesis, Delft Technical University.

Yu, R.C. et al. (2007). *“A comparative study between discrete and continuum models to simulate concrete fracture.”, Eng Fract Mech (2007), doi:10.1016/j.engfracmech.2007.03.031*

TABLE CAPTIONS

Table 1. SFRSCC containing 30 kg/m^3 of steel fibers: composition per m^3.

Table 2. Values of the fracture parameters defining the stress-strain softening laws.

Table 1. SFRSCC containing 30 kg/m^3 of steel fibers: composition per m^3.

Paste Volume [%]	*C* [kg/m^3]	*LF* [kg/m^3]	*W* [kg/m^3]	*SP* [kg/m^3]	*FS* [kg/m^3]	*CS* [kg/m^3]	*CG* [kg/m^3]
34	359.4	308.1	97.0	7.1	172.2	859.2	698.4

Table 2. Values of the fracture parameters defining the stress-strain softening laws.

Material	$\sigma_{I,1}^{cr}$ [MPa]	$\sigma_{I,2}^{cr}$ [MPa]	$\sigma_{I,3}^{cr}$ [MPa]	$\varepsilon_{I,2}^{cr} / \varepsilon_{I,ult}^{cr}$	$\varepsilon_{I,3}^{cr} / \varepsilon_{I,ult}^{cr}$	G_f^I [N/mm]
SFRSCC	3.50	1.750	2.065	0.009	0.150	4.300
Plain Concrete	3.50	0.525	-	0.072	-	0.087

FIGURE CAPTIONS

Fig. 1. Compression tests in specimens of distinct ages: (a) stress-strain and (b) rotation-strain relationships.

Fig. 2. Evolution with age of: (a) average compressive strength and (b) average elasticity modulus.

Fig. 3. Average load-deflection curves for specimens of distinct ages; (a) for a deflection up to 0.5 mm and (b) for a deflection up to 3.1 mm.

Fig. 4. Punching test on panel prototype: (a) test setup and (b) load-deflection experimental and numerical results.

Fig. 5. Flexural test on panel prototype: (a) test setup and (b) load-deflection experimental results.

Fig. 6. (a) Crack stress components, relative displacements and local coordinate system of the crack , (b) tri-linear stress-strain diagram to simulate the fracture mode I crack propagation of SFRSCC, and (c) generic out-of-plane (OP) shear stress-strain diagram to simulate mode III softening.

Fig. 7. Three-point notched beam flexural test at 7 days; (a) FEM mesh used in the numerical simulation and (b) obtained results.

Fig. 8. Punching test simulation; (a) upper face cracks predicted by the numerical model and (b) photograph showing the cracks at the upper face of the panel, after finishing the test sequence.

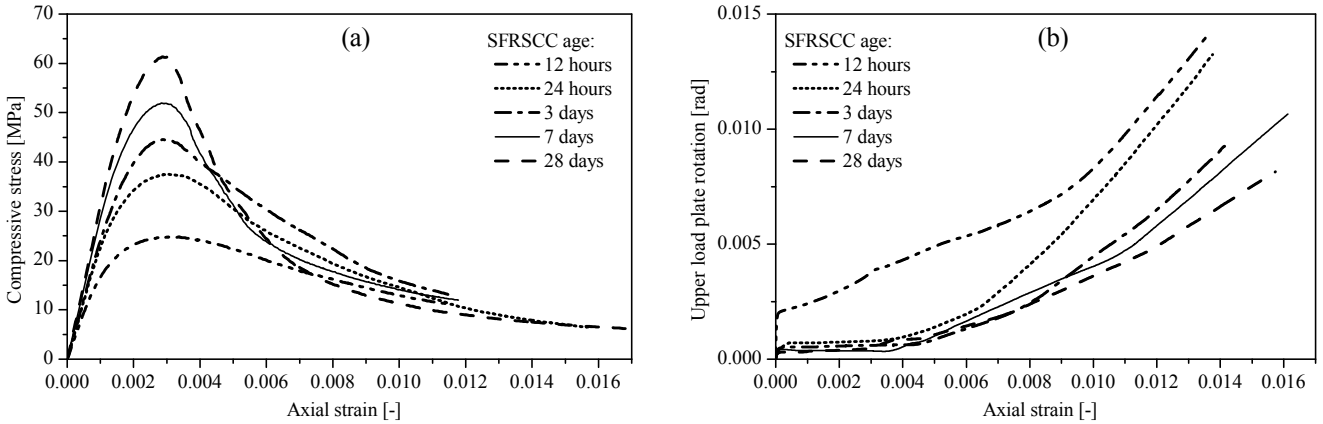

Fig. 1. Compression tests in specimens of distinct ages; (a) stress-strain and (b) rotation-strain relationships.

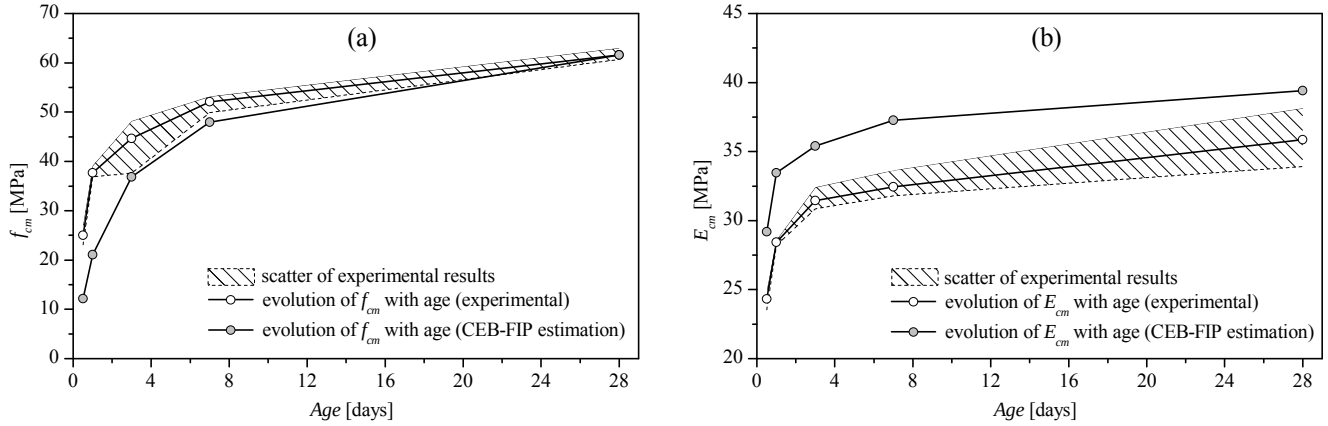

Fig. 2. Evolution with age of: (a) average compressive strength and (b) average elasticity modulus.

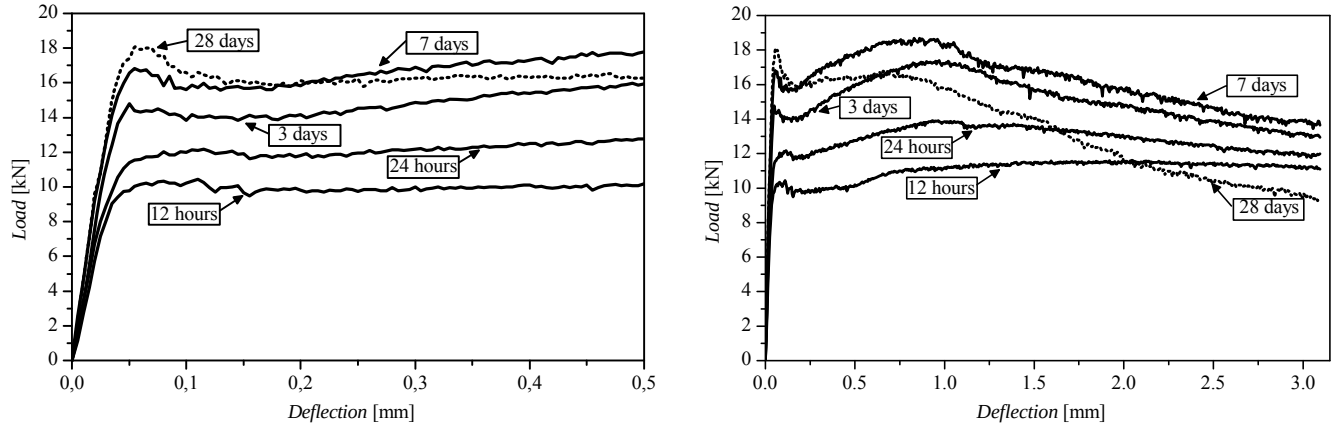

Fig. 3. Average load-deflection curves for specimens of distinct ages; (a) for a deflection up to 0.5 mm and (b) for a deflection up to 3.1 mm.

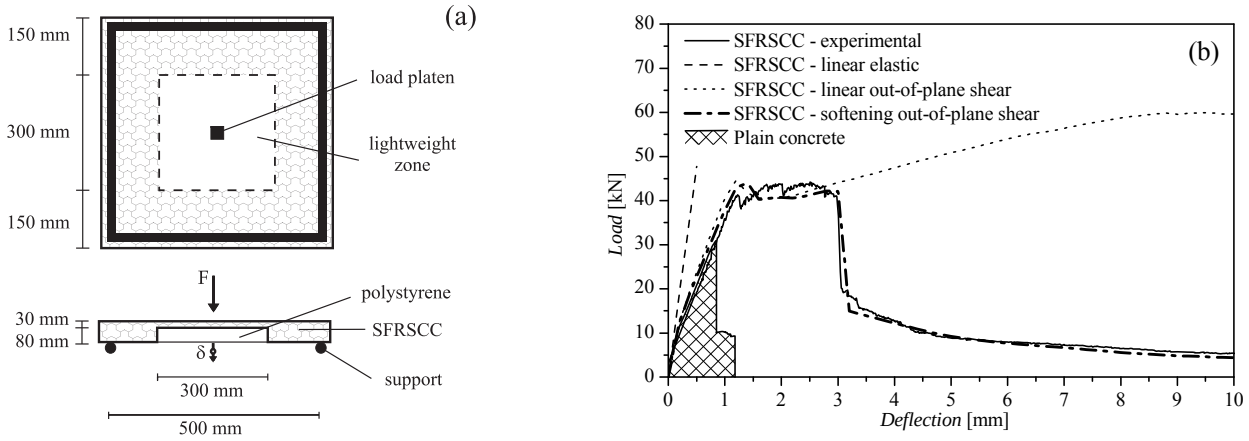

Fig. 4. Punching test on panel prototype; (a) test setup and (b) load-deflection experimental and numerical results.

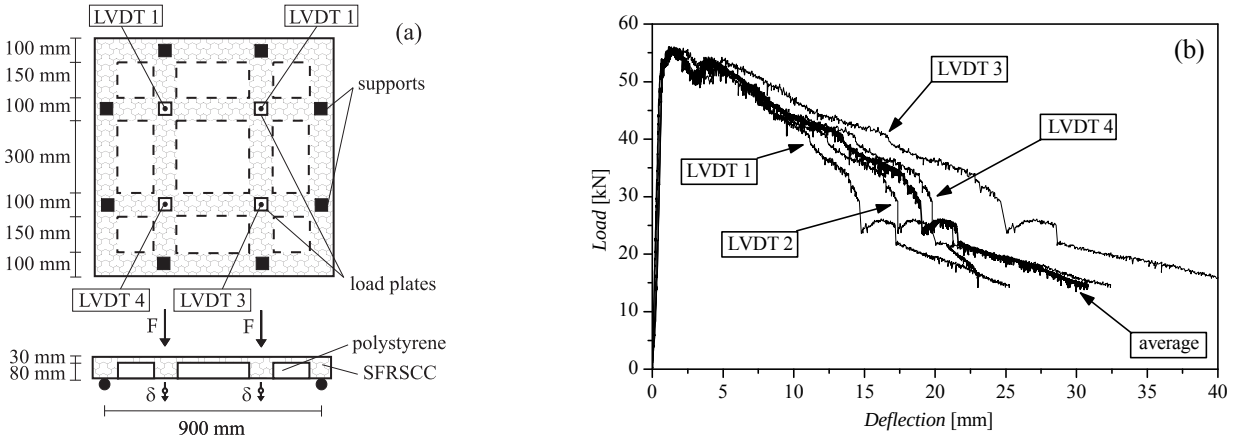

Fig. 5. Flexural test on panel prototype; (a) test setup and (b) load-deflection experimental results.

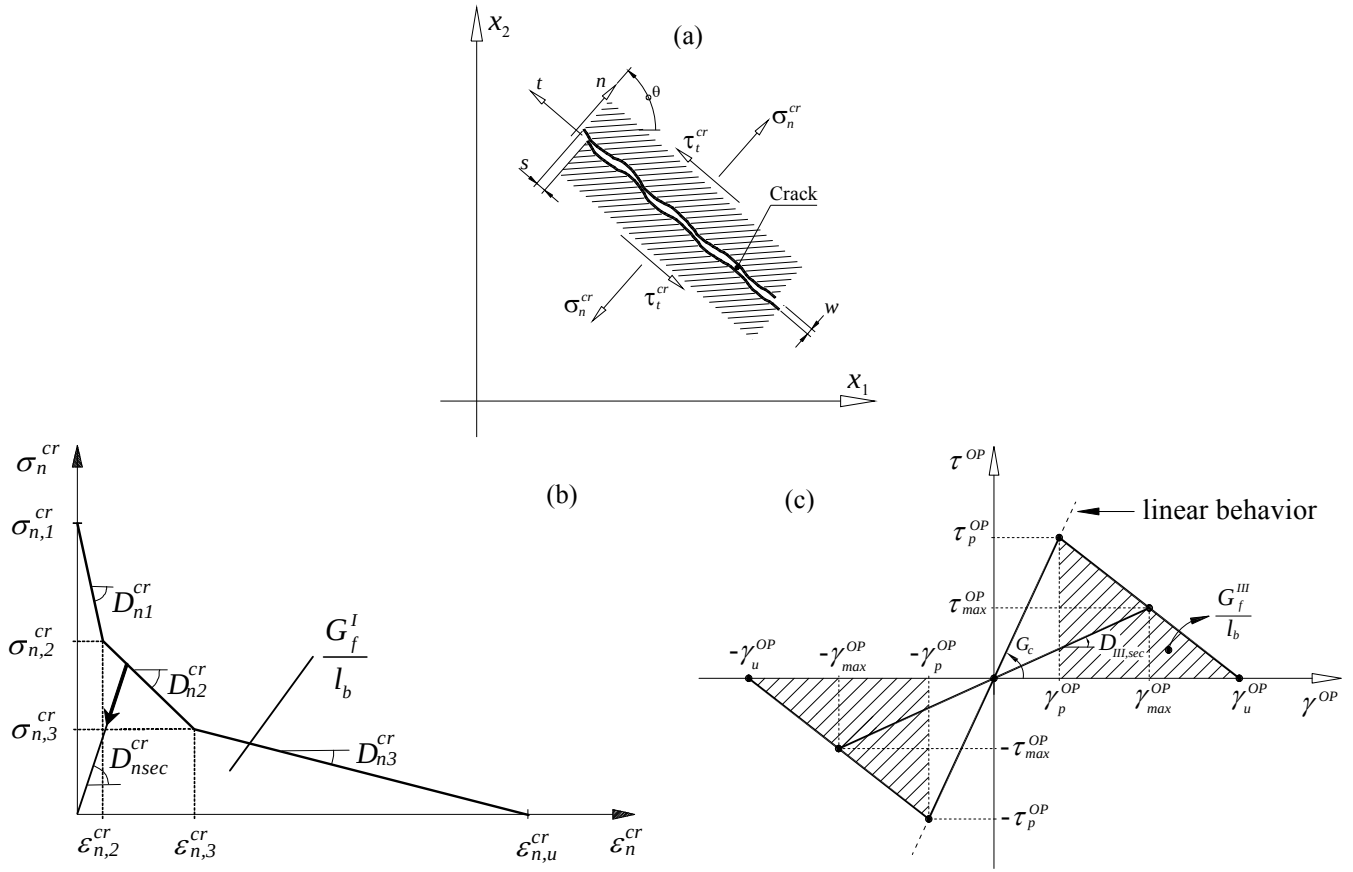

Fig. 6. (a) Crack stress components, relative displacements and local coordinate system of the crack , (b) tri-linear stress-strain diagram to simulate the fracture mode I crack propagation of SFRSCC, and (c) generic out-of-plane (OP) shear stress-strain diagram to simulate mode III softening.

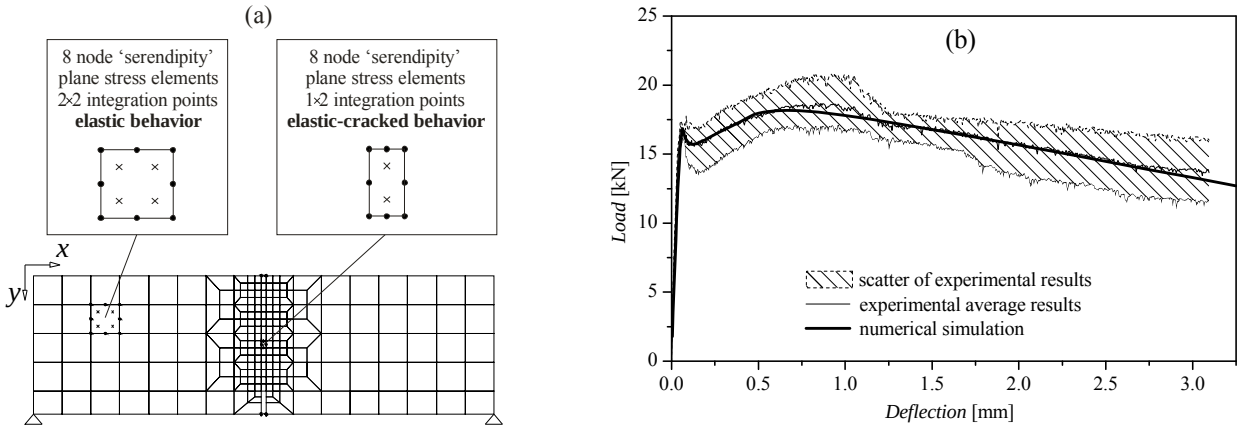

Fig. 7. Three-point notched beam flexural test at 7 days; (a) FEM mesh used in the numerical simulation and (b) obtained results.

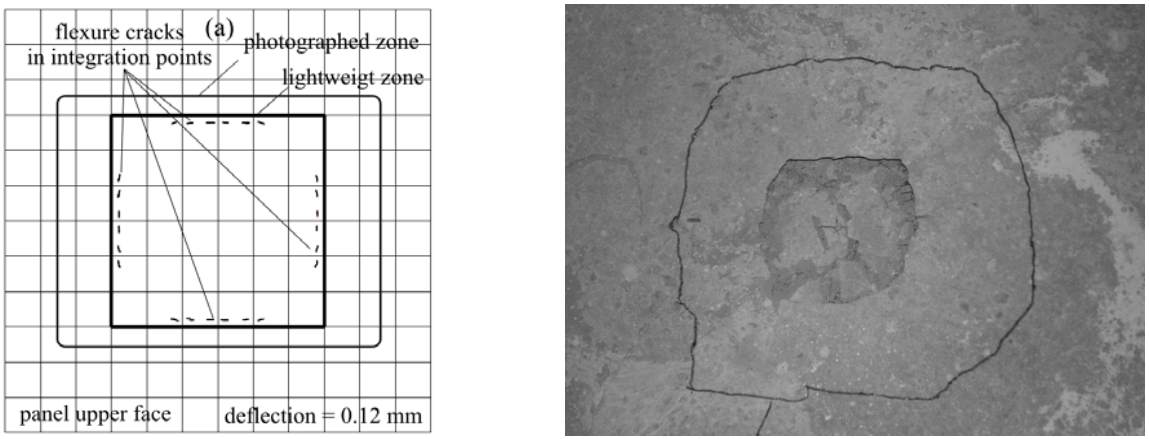

Fig. 8. Punching test simulation; (a) upper face cracks predicted by the numerical model and (b) photograph showing the cracks at the upper face of the panel, after finishing the test sequence.